Engineering 6 (2020) 1381–1394

Contents lists available at ScienceDirect

Engineering

journal homepage: www.elsevier.com/locate/eng

Research
Clean Power Technology—Review

Preparation of Nanoporous Carbonaceous Promoters for Enhanced CO_2 Absorption in Tertiary Amines

Masood S. Alivand [a,b], Omid Mazaheri [a,c], Yue Wu [a,b], Geoffrey W. Stevens [a,b], Colin A. Scholes [a,b], Kathryn A. Mumford [a,b,*]

[a] Department of Chemical Engineering, The University of Melbourne, Parkville, VIC 3010, Australia
[b] Peter Cook Centre for CCS Research, The University of Melbourne, Parkville, VIC 3010, Australia
[c] School of Agriculture and Food, Faculty of Veterinary and Agricultural Sciences, The University of Melbourne, Parkville, VIC 3010, Australia

ARTICLE INFO

Article history:
Received 13 January 2020
Revised 11 May 2020
Accepted 11 May 2020
Available online 30 May 2020

Keywords:
CO_2 absorption
Nanofluid
N,N-diethylethanolamine
Nanoporous carbonaceous promoters
Polyamine functionalization

ABSTRACT

Aqueous solutions of tertiary amines are promising absorbents for CO_2 capture, as they are typically characterized by a high absorption capacity, low heat of reaction, and low corrosivity. However, tertiary amines also exhibit very low kinetics of CO_2 absorption, which has made them unattractive options for large-scale utilization. Here, a series of novel nanoporous carbonaceous promoters (NCPs) with different properties were synthesized, characterized, and used as rate promoters for CO_2 absorption in aqueous *N*, *N*-diethylethanolamine (DEEA) solutions. To prepare a DEEA–NCP nanofluid, NCPs were dispersed into aqueous 3 mol·L^{-1} DEEA solution using ultrasonication. The results revealed that among microporous (GC) and mesoporous (GS) carbonaceous structures functionalized with ethylenediamine (EDA) and polyethyleneimine (PEI) molecules, the GC–EDA promoter exhibited the best performance. A comparison between DEEA–GC–EDA nanofluid and typical aqueous DEEA solutions highlighted that the GC-EDA promoter enhances the rate of CO_2 absorption at 40 °C by 38.6% (36.8–50.7 kPa·min^{-1}) and improves the equilibrium CO_2 absorption capacity (15 kPa; 40 °C) by 13.2% (0.69–0.78 mol of CO_2 per mole of DEEA). Moreover, the recyclability of DEEA–GC–EDA nanofluid was determined and a promotion mechanism is suggested. The outcomes demonstrate that NCP–GC–EDA in tertiary amines is a promising strategy to enhance the rate of CO_2 absorption and facilitate their large-scale deployment.

1. Introduction

Rising carbon dioxide (CO_2) emissions from global industrial sources have strengthened international concerns and scientific endeavors to reduce the impact of anthropogenic climate change [1,2]. The Paris Agreement in 2016 focused attention on reducing the growth in CO_2 emissions over the coming decades through a variety of mechanisms [3,4]. One viable approach is carbon capture and storage (CCS), which is strongly reliant on feasible CO_2 capture technologies. CCS will enable international governments to meet their Paris Agreement targets—especially in the industrial sector, including important industries such as ammonia and fertilizer production, cement kilns, as well as iron and steel manufacturing. Among the different CO_2 absorption techniques that are currently available (e.g., absorption [5–7], adsorption [8–10], membrane separation [11,12], and condensation [13,14]), chemical absorption using aqueous amine solutions has been the most commercially successful technology for CO_2 capture from flue gas (post-combustion carbon capture) and natural gas sweetening [15,16].

Monoethanolamine (MEA), diethanolamine (DEA), and methyldiethanolamine (MDEA) are commonly used primary, secondary, and tertiary amines for large-scale CO_2 absorption applications. Both primary and secondary amines are able to directly react with CO_2 molecules and produce carbamate, which is considered a fast reaction and can significantly increase the kinetics of CO_2 absorption during continuous operation. Nonetheless, the carbamate formation mechanism in primary and secondary amine solutions causes a relatively low CO_2 absorption capacity (1:2 stoichiometry up to 0.5 mol CO_2 per mole amine) in which one molecule of CO_2 reacts with two molecules of amine. Thus, both MEA and DEA benefit from fast kinetics of CO_2 absorption, which differentiates them from the tertiary amine candidates. However, these

* Corresponding author.
E-mail address: mumfordk@unimelb.edu.au (K.A. Mumford).

https://doi.org/10.1016/j.eng.2020.05.004
2095-8099/

compounds suffer from a high heat of regeneration, corrosion, and oxidation problems [17,18]. On the other hand, in tertiary amine solutions, one molecule of CO_2 reacts with one molecule of amine and forms bicarbonate, which provides a high absorption capacity (1:1 stoichiometry up to 1 mole CO_2 per mole amine). Therefore, the tertiary amine MDEA has a high CO_2 absorption capacity, low heat of regeneration, and considerable resistance against chemical oxidation [19,20]. However, the slow kinetics of CO_2 absorption in aqueous MDEA solution—or in tertiary amine solutions in general—has substantially inhibited its commercial development.

In 2007, Vaidya and Kenig [21] introduced *N*,*N*-diethylethanolamine (DEEA) as a substitute for MDEA with a higher CO_2 absorption rate. Afterward, Chowdhury et al. [22,23] evaluated the absorption properties of 26 different tertiary amines and demonstrated that DEEA has a higher CO_2 absorption rate, higher cyclic CO_2 absorption capacity, and lower heat of absorption compared with conventional MDEA. Nevertheless, the study supported the conclusion that the kinetics of CO_2 absorption in both MDEA and DEEA are not comparable with primary or secondary amines.

To take advantage of the properties of tertiary amines, research endeavors have focused on overcoming their low CO_2 absorption rate by adding primary and secondary amines. Hafizi et al. [19] investigated the efficiency of different polyamines as active promoters for MDEA solutions. Similarly, Gao et al. [6] studied the effect of different amine activators on the CO_2 absorption rate of aqueous DEEA solutions. The results revealed that, although amine promoters can effectively increase the kinetics of CO_2 absorption, they can also considerably increase the required heat of regeneration, corrosion activity, and chemical oxidation. Recently, it was established that using metal oxide nanoparticles and carbon-based nanomaterials in an aqueous solution of tertiary amines can promote the CO_2 absorption capacity and kinetics of CO_2 absorption without introducing the drawbacks of amine promoters.

Rahmatmand et al. [24] displayed that the addition of only 0.02 wt% carbon nanotube (CNT) enhanced the CO_2 absorption capacity of MDEA solution up to 23%. Komati and Suresh [25] showed that the presence of Fe_3O_4 nanoparticles in MDEA solutions is capable of decreasing the mass transfer resistance at the liquid-gas interface and enhancing mass transfer. Irani et al [20] and Maleki et al [26] investigated the CO_2 and H_2S absorption using aqueous MDEA solution in the presence of pristine graphene oxide (GO) and amine-functionalized graphene oxide (GO–NH_2). They pointed out that the CO_2 absorption enhancement of pristine GO-promoted MDEA solution is governed by a physical promotion mechanism that takes advantage of the nanofluids. On the other hand, GO–NH_2-promoted MDEA solution not only benefits from the physical absorption improvement mechanism of the nanofluids, but also takes advantage of chemical absorption promotion. Tavasoli et al. [26] showed that the primary amine functional groups located on the surface of GO can actively react with CO_2 molecules, enhance CO_2 absorption capacity, and promote CO_2 absorption rate in aqueous MDEA solvent.

However, due to the low surface area and porosity of GO, the number of active primary amine groups is limited, which negatively affects its chemical promotion efficiency. Importantly, the present research highlights the potential of amine-functionalized nanoporous nanoparticles to act as a promoter for the DEEA system. Accordingly, this investigation focuses on the synthesis of nanoporous carbonaceous promoters (NCPs) derived from commercial activated carbon samples with high surface area and different surface functionalities, which make them unique candidates for the preparation of amine-based nanofluids. The synthesized NCPs were post-functionalized by two different polyamines—ethylenediamine (EDA) and polyethylenimine (PEI)—both of which have the primary amine moiety that is needed to act as a promoter. This study therefore investigated the active primary/secondary amine groups on the accessible surface area of nanoporous carbon structure; and determined the improvement to CO_2 absorption capacity as well as increase in the rate of CO_2 absorption in the aqueous DEEA solution.

2. Materials and methods

2.1. Materials

Coconut-shell-based microporous (GC) activated carbon (Acticarb GC1200 GAC) and coal-based mesoporous (GS) carbon (Acticarb GS1300 GAC) were purchased from Activated Carbon Technologies Pty. Ltd. (Australia) and used as the carbon source. DEEA 99.5%, 4-dorpholineethanesulfonic acid (MES, 99.5%), 4-morpholinepropanesulfonic acid (MOPS, 99.5%), EDA, and branched PEI (M_W = 25 000, 99%) were all purchased from Sigma-Aldrich LLC. (Germany). 1-ethyl-3-(3-dimethylaminopropyl) carbodiimide hydrochloride (EDC, 99%) and *N*-hydroxysuccinimide (NHS, 99%) were obtained from Proteochem (USA). Nitric acid (HNO_3, 70%) and sulfuric acid (H_2SO_4, 98%) were provided by Chem-Supply Ltd. (Australia). Ultra-pure nitrogen (N_2, 99.9%) and carbon dioxide (CO_2, 99.9%) were supplied by BOC Gases Australia Ltd. and used for CO_2 absorption experiments. Deuterium oxide (D_2O, 99.9%), acetonitrile (AN, 99.9%), and nuclear magnetic resonance (NMR) tubes were purchased from Sigma-Aldrich. All chemicals were used as received without further treatment.

2.2. Synthesis of oxidized NCPs (NCP–COOH)

To synthesize the oxidized NCPs from commercial granular activated carbon (GAC), 2 g of GAC was washed several times with deionized (DI) water, dried at 60 °C in a vacuum oven overnight, and completely crushed by a grinder into a fine powder. The resultant fine activated carbon powder was placed in a round flask and mixed with 100 mL of concentrated HNO_3. Due to the exothermic oxidation reaction between HNO_3 and the high-surface-area activated carbon, HNO_3 was gradually added into the flask at room temperature. To improve the oxidation ability of HNO_3, 40 mL of H_2SO_4 was slowly added as a strong oxidation promoter to the mixture under vigorous stirring provided by an external magnetic stirrer. Activated carbon powder was further dispersed in the HNO_3/H_2SO_4 mixture by ultrasonication for 2 h. The obtained mixture was heated to 85 °C and refluxed at this temperature for 12 h. Following this, the product was diluted by 1000 mL of water; the supernatant liquid was then separated and filtered using a sintered glass funnel and washed with a copious amount of boiling water until a neutral pH was obtained. The residue was separated and dried using a vacuum oven at 60 °C overnight. It was labeled as NCP–GC–COOH for the microporous structure and NCP–GS–COOH for the mesoporous structure.

2.3. Synthesis of amine-functionalized NCPs (NCP–NH_2)

Amine functionalization of the NCP–COOH samples was carried out in two consecutive steps using the EDC–NHS cross-linking method to couple the amine groups of polyamines onto the carboxylic groups of NCP–COOH. Briefly, 1.5 g of NCP–COOH was dispersed in 1000 mL of MES buffer (0.1 $mol \cdot L^{-1}$ and pH 5.5) and ultrasonicated for 15 min to obtain a uniform solution. Next, 3.3 g of EDC and 2 g of NHS were slowly added to the mixture and gently stirred for 18 h at room temperature in the absence of light. The resultant mixture was subsequently filtered using a sintered glass funnel and washed with DI water to completely

remove unreacted EDC/NHS molecules on the porous structure. In the second step, the filtered NCP sample with amine-reactive NHS ester groups (NCP–NHS) was suspended in 500 mL MOPS buffer (0.1 mol·L^{-1} and pH 7.5) and ultrasonicated for 15 min to make a homogeneous solution. Afterward, 500 mL of aqueous EDA or PEI solution (10 mg·mL^{-1}) was mixed with the solution and stirred for an additional 12 h at room temperature to graft amine-reactive NHS ester groups onto the surface of the NCPs. At the end, after the conjunction of the polyamines to the amine-reactive NHS ester groups of NCP–NHS, the reaction mixture was filtered, washed with DI water to remove unreacted amines, dried at 60 °C overnight, and labeled as NCP–X–Y, where X represents the porosity type of the sample (GC or GS) and Y indicates the grafted polyamine on the surface (EDA or PEI). For example, NCP–GC–EDA refers to a microporous carbon-based promoter with grafted EDA molecules on the surface. The reaction pathway for the conjunction of the polyamines on the surface of NCP is schematically illustrated in Fig. 1.

2.4. Characterization

Fourier-transform infrared spectroscopy (FT-IR) spectra in the range of 400–4000 cm^{-1} were collected using a Bruker Tensor II (Bruker Corporation, USA) in attenuated total reflection (ATR) mode to detect chemical bonding and functional groups. The elemental composition of the samples was determined by a LECO TruMac CNS analyzer (LECO, USA). To indirectly measure the amount of functional groups, thermogravimetric analysis (TGA) and differential thermogravimetry (DTG) were undertaken using a NETZSCH TG 209 F1 Libra analyzer (NETZSCH Holding, Germany) heated from 30 to 850 °C with a heating rate of 10 °C·min^{-1} in N_2 stream. X-ray photoelectron spectroscopy (XPS) was carried out on a VG ESCALAB 220i-XL spectrometer (Thermo Fisher Scientific, USA) under severe vacuum pressure (10^{-7} Pa) with A1 Kα radiation and a fixed photon energy of 1486.6 eV. In addition to a broad survey scan in the 0–1400 eV range with 1.0 eV resolution, high-resolution scans for C 1s (282–294 eV), N 1s (396–408 eV), and O 1s (528–538 eV) were conducted with 0.05 eV resolution. Raman spectra were obtained with a Renishaw inVia Qontor confocal Raman microscope system (Renishaw, India) with a laser excitation wavelength of 532 nm, spectral resolution of 1 cm^{-1}, and over 800–3200 cm^{-1} range. To effectively immobilize the carbon powder during the operation of the Raman instrument, the samples were dispersed in ethanol, coated on a silicon wafer, and dried under vacuum at ambient temperature for 2 h. Scanning electron microscopy (SEM) images were taken by an FEI Quanta 200 ESEM FEG instrument (USA), with 20 and 30 kV operation voltages. Zeta potential and dynamic light scattering (DLS) measurements were performed by a Malvern Zetasizer Nano ZS (Malvern Panalytical Ltd., UK) equipped with a He–Ne ion laser (λ = 633 nm). The species formed during CO_2 absorption in the amine solution were identified by NMR spectroscopy analysis (Agilent 500 MHz; Agilent Technologies, Inc., USA). The delay time and number of scans were set at 20 s and 128, respectively, for ^{13}C NMR, and at 2 s and 32, respectively, for ^{1}H NMR measurement. Each NMR tube contained 600 μL D_2O (as a solvent), 100 μL sample, and 10 μL acetonitrile (as an internal reference). The surface area and pore volume were measured by a Micrometrics 3Flex instrument (MicroMetrics, USA) using the N_2 adsorption technique at 77 K. A BS/IP/RF U-tube reverse-flow capillary viscometer (ASTM D445-06) was employed to measure the viscosity of the amine solutions and the prepared nanofluids.

2.5. Preparation of DEEA–NCP nanofluid

The concentration of aqueous DEEA solution was kept constant at 3 mol·L^{-1} for all experiments. 350 g of DEEA was dissolved in DI water and diluted until a 1 L volume of solution was obtained. To prepare the DEEA–NCP nanofluid, typically 0.1 g of NCP sample was weighed, dispersed in 100 mL of aqueous 3 mol·L^{-1} DEEA solution and ultrasonicated for 30 min. The obtained nanofluids were labeled as DEEA–X–Y, where X defines the porosity type of NCP

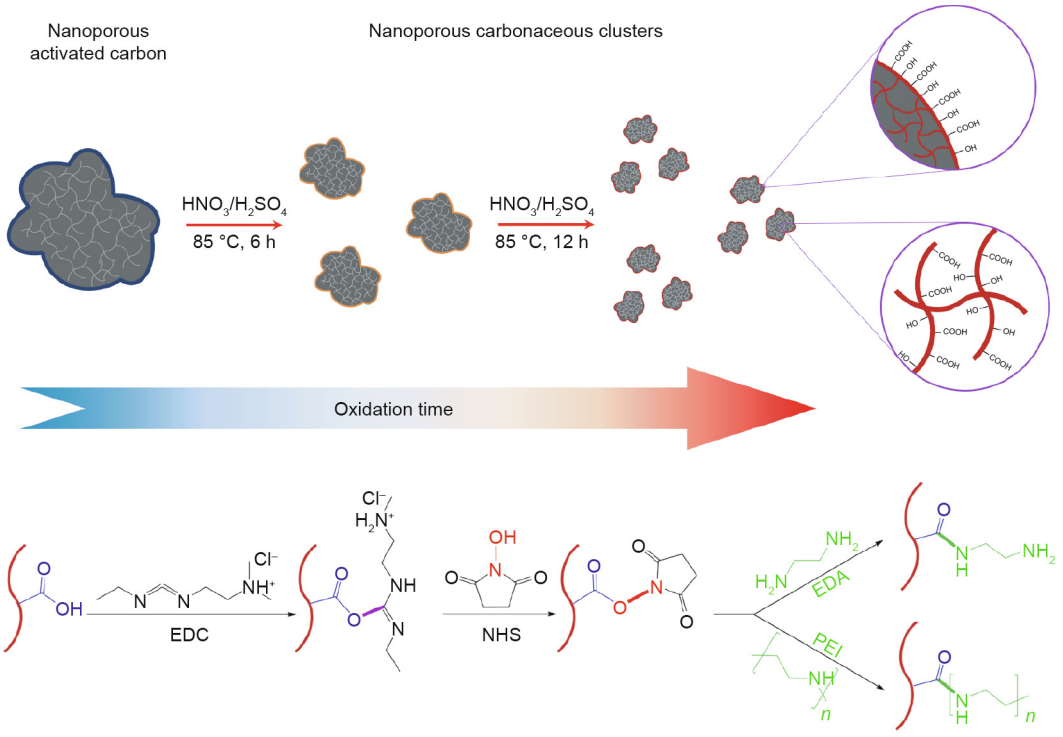

Fig. 1. Schematic diagram for the synthesis of NCPs and polyamine grafted NCPs.

(i.e., GC or GS), and Y defines the surface functionalities of NCP (i.e., COOH, EDA, or PEI).

2.6. Measurement of CO_2 absorption

In order to quantitatively monitor the absorption of CO_2 into the prepared nanofluids, an in-house vapor–liquid equilibrium (VLE) apparatus was used. The details of operation and measurement accuracy have been presented in our previous works [5,27]. A simple schematic diagram of the CO_2 absorption apparatus is presented in Fig. 2. In a typical CO_2 absorption experiment, 100 mL of nanofluid was weighed and loaded in the stainless-steel reactor with 325 mL available volume. Afterward, the reactor was completely sealed, put into a water bath, and connected to the gas injection system. Before starting the CO_2 absorption experiments, the system was purged with pure N_2 at 70 °C for 15 min to remove dissolved air and other unwelcome gas molecules from the loaded DEEA–NCP nanofluid. The reactor was then pressurized with pure N_2 to 175 kPa, and the water bath temperature was set at a desired operational temperature (typically 40 °C) for CO_2 absorption. When the reactor temperature set-point was reached and its pressure was stabilized, the buffer tank (500 mL) was pressurized with pure CO_2 gas and the final pressure was recorded (P_1). After that, the pressurized CO_2 was injected from the buffer tank to the reactor and the new pressure of the buffer tank was again recorded (P_2).

To dynamically monitor and record the pressure of the apparatus, two micro silicon pressure sensor transducers with high accuracy (0.08% of full-scale) were installed on each of the CO_2 buffer tank (Omega, PX409-150 GUSBH, 0–1030 kPa) and the reactor (OMEGA, PX409-100 GUSBH, 0–690 kPa; OMEGA Engineering Inc., UK). The water bath was equipped with a digital immersion heater circulator (Ratek, TH7000; Ratek Instruments, Australia) with high accuracy to control the temperature of the water bath, and a thermocouple (Omega, TJ-USB-K1; OMEGA Engineering Inc., UK) with ±0.1 °C accuracy was used to monitor the reactor temperature.

The total number of moles of CO_2 injected into the VLE reactor can be directly calculated by Eq. (1):

$$n_{CO_2} = \frac{V_{BT}P_1}{RT_aZ_1} - \frac{V_{BT}P_2}{RT_aZ_2} \tag{1}$$

where P_1 and P_2 are the pressure of the CO_2 buffer tank before and after CO_2 injection; V_{BT} is the available volume of the buffer tank; T_a is the ambient temperature; R is the ideal gas constant; and Z_1 and Z_2 are the compressibility factor of CO_2 corresponding to the P_1 and P_2 pressures.

To calculate the compressibility factor at different CO_2 partial pressures, the Soave–Redlich–Kwong (SRK) equation of state was employed (Eq. (2)) [1]:

$$Z^3 - Z^2 + \left(\frac{aP - b^2P^2}{R^2T^2} - \frac{bP}{RT}\right)Z = \frac{abP^2}{R^3T^3} \tag{2}$$

where P is the pressure; T is the temperature; Z is the compressibility factor. All necessary coefficients can be obtained by Eqs. (3)–(5):

$$a = 0.4274\frac{R^2T_c^2}{P_c}\left[1 + m(1 - \sqrt{T_r})\right]^2 \tag{3}$$

$$b = 0.0866\frac{RT_c}{P_c} \tag{4}$$

$$m = 0.48 + 1.574\omega - 0.176\omega^2 \tag{5}$$

where T_c is the critical temperature, T_r is the reduced temperature, P_c is the critical pressure, and ω is the acentric factor.

The partial pressure of CO_2 in the VLE reactor (P_{CO_2}) can be calculated by Eq. (6):

$$P_{CO_2} = P_R - P_I \tag{6}$$

where P_R is the reactor pressure and P_I is the initial N_2 pressure injected in the VLE reactor.

Accordingly, the total number of moles of CO_2 in the gas ($n^g_{CO_2}$, Eq. (7)) and liquid ($n^l_{CO_2}$, Eq. (8)) phases is obtained by the following:

$$n^g_{CO_2} = \frac{V_gP_{CO_2}}{Z_{CO_2}RT_R} \tag{7}$$

$$n^l_{CO_2} = n_{CO_2} - n^g_{CO_2} \tag{8}$$

where V_g is the gas volume in the reactor, T_R is the adjusted reactor temperature, and Z_{CO_2} is the compressibility factor corresponding to the P_{CO_2}.

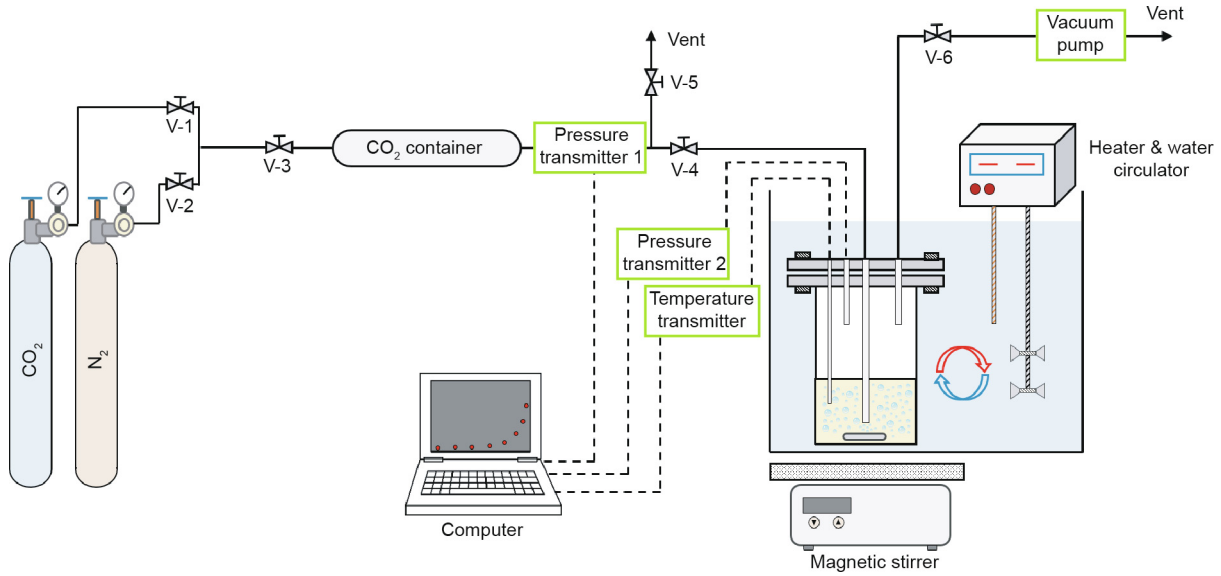

Fig. 2. Schematic diagram of the vapor–liquid equilibrium (VLE) rig for CO_2 absorption measurement.

The total amount of absorbed CO_2 into the loaded DEEA–NCP nanofluid during each CO_2 injection cycle is computed by Eqs. (9) and (10):

$$m_{CO_2} = \frac{n^{l}_{CO_2}}{w_{sol}} \tag{9}$$

$$\alpha_{CO_2} = \frac{n^{l}_{CO_2}}{n_{amine}} \tag{10}$$

where m_{CO_2} is the molality of CO_2 (mole of CO_2 per kilogram of amine solution); α_{CO_2} is the CO_2 loading (mole of CO_2 per mole of amine); w_{sol} is the weight of the solution (kg); and n_{amine} is the total number of moles of amine in the solution.

To measure the rate of CO_2 absorption and CO_2 absorption rate enhancement after adding nanoporous carbonaceous promoters, Eqs. (11) and (12) were employed, respectively.

$$R_{CO_2} = \frac{1}{6}\sum_{i=1}^{6}\left[\left(\frac{\partial P}{\partial t}\right)_{\Delta P_i}\right]_{Amine} \times 100\% \tag{11}$$

$$\text{Enhancement} = \frac{1}{6}\sum_{i=1}^{6}\frac{\left[\left(\frac{\partial P}{\partial t}\right)_{\Delta P_i}\right]_{Nanofluid}}{\left[\left(\frac{\partial P}{\partial t}\right)_{\Delta P_i}\right]_{Amine}} \times 100\% \tag{12}$$

where R_{CO_2} is the rate of CO_2 absorption (kPa·min^{-1}); P is the operating pressure (kPa); t is the time (min); and ΔP (i.e., 50, 100, 150, 200, 250, and 300 kPa) is the pressure drop after starting the gas absorption experiment (kPa).

For cyclic CO_2 absorption–desorption experiments, the CO_2-saturated DEEA–NCP nanofluid was poured into a round flask and heated at 95 °C for 3 h under reflux conditions. Next, the regenerated DEEA–NCP nanofluid was naturally cooled down to room temperature and used again for CO_2 absorption experiments. The regeneration efficiency was defined as follows:

$$\text{Regeneration efficiency} = \frac{[R_{CO_2}]_i}{[R_{CO_2}]_{Fresh}} \times 100\% \tag{13}$$

where i is the number of each cycle.

3. Results and discussion

3.1. Characterization of NCPs

The FT-IR spectra of all commercial activated carbons and synthesized NCPs are illustrated in Figs. 3(a) and (b). In brief, the absorbance bands centered on 1750 and 1150 cm^{-1} were ascribed to the vibration of C=O and C–O bonds, respectively [28,29]. In addition, the prominent absorbance at around 1570 and 1380 cm^{-1} corresponded to the N–O and C–N stretching vibrations [29,30]. Compared with commercial activated carbons (i.e., AC–GC and AC–GS), the spectra of NCP–GC–COOH and NCP–GS–COOH had stronger absorbance bands for all four C=O, C–O, N–O, and C–N vibrations. To be specific, the intensification of the C=O/C–O and N–O/C–N characteristic peaks implies the successful implantation of carboxylic (–COOH) and nitrous ($–NO_2$) functional groups on the surface of nanoporous carbon as the direct result of HNO_3 oxidation/nitration [30,31]. After EDA and PEI functionalization using EDC–NHS cross-linking agents, the intensity of the absorption band related to the carbonyl bond (C=O) was significantly reduced. Similarly, the intensity of the C–O vibrational bands located at 1150 cm^{-1} decreased after the conjunction of polyamines on the previously implanted carboxylic groups. These observations confirm the polyamine immobilization on the surface of the nanoporous carbon through the successful conversion of carboxylic groups to amide groups using EDC–NHS cross-linker [32–35].

To gain additional information on the attached functional groups on the surface of the synthesized NCPs, we report on the combination of TGA/DTG and elemental analysis. According to the TGA (Fig. S1 in Appendix A) and DTG (Fig. S2 in Appendix A) curves of the commercial activated carbons and functionalized NCPs, the weight loss can be categorized into three different regions. The first weight-loss region was observed around 90–110 °C and was due to moisture evaporation [10]. The decomposition of oxygen-containing functional groups (i.e., –COOH and –OH) started at 180 °C and continued to higher temperatures. In addition to the decomposition of oxygen groups at 300–330 °C, another peak was observed in the EDA- and PEI-grafted NCP samples (see Fig. S1 and Fig. S2) and continued until 600 °C; this was mainly due to the decomposition of amine groups [30]. Hence, the weight loss between 180 and 600 °C was considered to be an indicator of the amount of functional groups. The results are presented in Figs. 3(c) and (d). Pristine AC–GC and AC–GS exhibited 4.9% and 2.1% weight reduction, respectively, which can be ascribed to their inherent carboxyl (–COOH) and carbonyl (–OH) functional groups. Nevertheless, the weight reduction of HNO_3-oxidized NCP–GS–COOH (20.0 wt%) was considerably higher than that of NCP–GC–COOH (12.7 wt%). Interestingly, after polyamine grafting, the microporous NCP–GC–EDA displayed greater weight reduction (18.1 wt%) than the NCP–GC–PEI (17.4 wt%), while the polyamine-functionalized mesoporous NCP–GS showed a contrary behavior. The weight reduction of mesoporous EDA-grafted NCP–GS–EDA (20.2 wt%) was 27.7% less than that of PEI-grafted NCP–GS–PEI (25.8 wt%). It seems that the PEI molecules failed to effectively enter the micropores of the NCP–GC structure due to their high molecular weight and large radius of gyration, while the EDA molecules successfully loaded the micropores with high grafting conversion. Similarly, the results of the elemental analysis for different NCP samples (Table 1) proved the presence of inherent oxygen functional groups on the surface of commercial AC–GS carbon, remarkable enrichment of oxygen content after HNO_3 oxidation (i.e., NCP–GC–COOH and NCP–GS–COOH), and nitrogen content after polyamine conjunction (i.e., NCP–GC–EDA, NCP–GC–PEI, NCP–GS–EDA, and NCP–GS–PEI) on the surface, all of which are compatible with the previously presented interpretations.

Table 1 shows the textural properties of ACs (i.e., AC–GC and AC–GS) and the prepared NCP promoters. As can be seen, although the coal-based AC–GS sample possessed a greater specific surface area (SSA) (1425.17 m^2·g^{-1}) and pore volume (0.93 cm^3·g^{-1}) than the coconut-based AC–GC (1137.41 m^2·g^{-1} and 0.46 cm^3·g^{-1}), its pore volume and SSA were remarkably affected by surface oxidation and decreased to 263.75 m^2·g^{-1} and 0.16 cm^3·g^{-1} in NCP–GS–COOH. In comparison, the NCP–GC–COOH promoter displayed a highly accessible SSA (860.82 m^2·g^{-1}) and pore volume (0.47 cm^3·g^{-1}), making it a better porous base for amine grafting. Hence, NCP–GC–EDA (227.28 m^2·g^{-1} and 0.13 cm^3·g^{-1}) and NCP–GS–PEI (9.78 m^2·g^{-1} and 0.01 cm^3·g^{-1}) respectively exhibited the best and worst textural properties among the four polyamine grafted promoters.

To further explore the structure of ACs and NCP samples, Raman spectroscopy was employed (Figs. 4(a) and (b)). All samples exhibited two peaks around 1350 cm^{-1} (D band) and 1590 cm^{-1} (G band), which were both characteristic indicators of the carbon structure. The D band shows the sp^3 disordered/amorphous mode and the G band corresponds to the sp^2 bond stretching of the carbon structure [29,30,36]. Therefore, the intensity ratio of the D band to the G band (I_D/I_G) can representatively indicate structural disorder in carbon-based nanomaterials (see Table S1 in Appendix A). Both AC–GC (1.12) and AC–GS (1.14) displayed high I_D/I_G values, indicating a high degree of defect in the structure of commercial

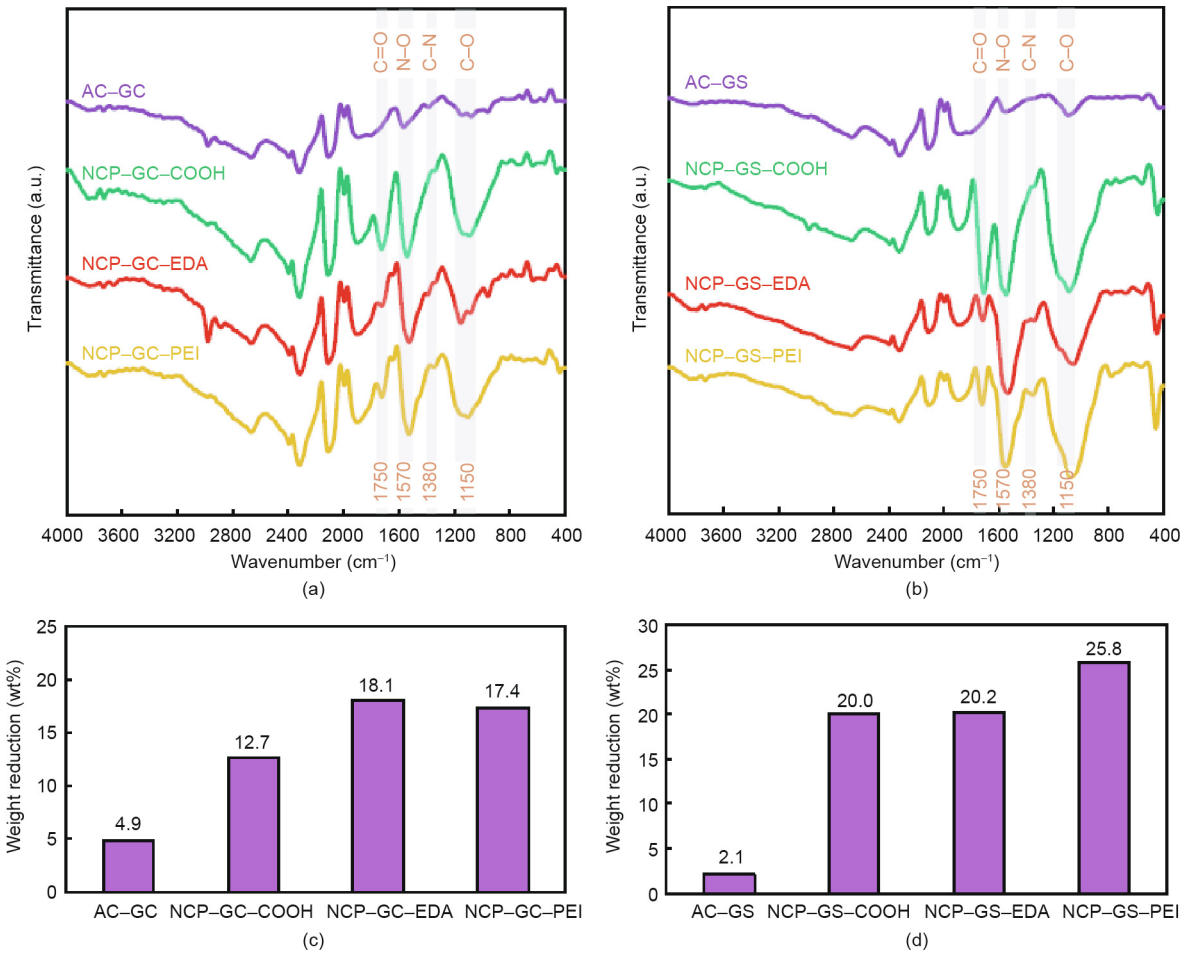

Fig. 3. (a, b) FT-IR spectra and (c, d) TGA weight reduction between 180 and 600 °C under N_2 atmosphere for the synthesized NCPs.

Table 1
Textural properties and elemental analysis of different prepared AC and NCP samples.

Sample	Textural properties				Elemental content (wt%)		
	SSA ($m^2 \cdot g^{-1}$)	Micropore volume ($cm^3 \cdot g^{-1}$)	Mesopore volume ($cm^3 \cdot g^{-1}$)	Total pore volume ($cm^3 \cdot g^{-1}$)	C	N	O
AC–GC	1137.41	0.46	–	0.46	99.6	0.08	0.28
NCP–GC–COOH	860.82	0.37	0.10	0.47	83.09	0.46	14.81
NCP–GC–EDA	227.28	0.08	0.05	0.13	86.79	5.01	7.38
NCP–GC–PEI	56.31	0.01	0.03	0.04	85.84	3.93	9.21
AC–GS	1425.17	0.44	0.49	0.93	90.63	0.17	8.28
NCP–GS–COOH	263.75	0.06	0.10	0.16	70.36	0.69	26.05
NCP–GS–EDA	33.32	–	0.03	0.03	66.41	7.03	17.91
NCP–GS–PEI	9.78	–	0.01	0.01	63.56	8.55	19.11

microporous and mesoporous activated carbons. After surface oxidation with HNO_3, the I_D/I_G value decreased in the NCP–GC–COOH (1.04) and NCP–GS–COOH (0.96) samples, which can be ascribed to the partial graphitization of the porous carbon structure under the harsh oxidation conditions [37]. However, the reduced I_D/I_G values of NCP–GC–COOH and NCP–GS–COOH are still comparable with those previously reported in the literature [8,28–30]. On the other hand, the I_D/I_G ratio increased from NCP–GC–COOH (1.04) to NCP–GC–EDA (1.06) and NCP–GC–PEI (1.07) when polyamines were immobilized through the structure of the nanoporous carbon. In a similar trend, both polyamine-functionalized NCP–GS–EDA (1.05) and NCP–GS–PEI (0.98) exhibited a higher I_D/I_G ratio than that of NCP–GS–COOH (0.96), indicating that new defects were created by grafted polyamines on the surface.

In addition to the FT-IR, TGA, and elemental analysis, XPS was utilized as a quantitative surface analysis technique to measure the amount of different functional groups on the surface of the NCPs. The XPS survey spectra and the amount of oxygen/nitrogen species on the surface of NCP–GC–COOH and NCP–GC–EDA, as the representative NCPs, are depicted in Fig. 4(c). In the XPS survey spectra (Fig. 4(c)), three major peaks were recorded at around 285, 397, and 532 eV, which represent C 1s, N 1s, and O 1s [38]. As the total atomic analysis (Fig. 4(d)) of the surface shows, the oxygen content decreased from 14.55 at% in NCP–GC–COOH to 12.46 at%

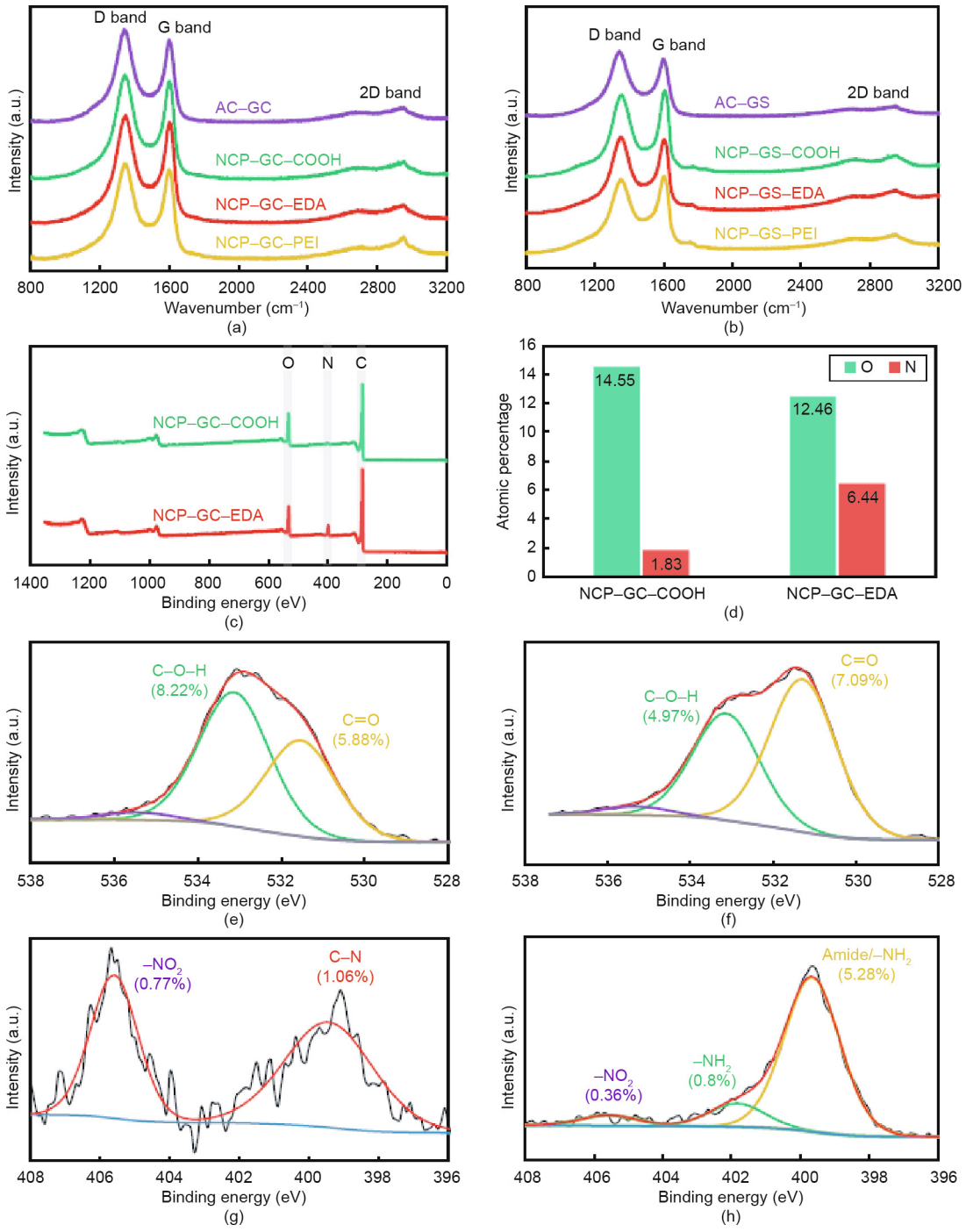

Fig. 4. Raman spectra of (a) microporous and (b) mesoporous samples, (c) full XPS survey, (d) quantitative elemental analysis, high-resolution, (e, f) O 1s and (g, h) N 1s spectra of NCP–GC–COOH and NCP–GS–EDA nanopromoters.

in NCP–GC–EDA, whereas the nitrogen content increased from 1.83 at% in NCP–GC–COOH to 6.44 at% in NCP–GC–EDA; these results superficially ratify amine conjunction on the surface through amide formation. To scrutinize the amine functionalization mechanism, high-resolution spectra of different moieties were recorded (Figs. 4(e)–(h) and Fig. S3 in Appendix A). According to Fig. 4(e), the NCP–GC–COOH sample possessed two C–O–H (8.22 at%; 533.2 eV) and C=O (5.88%; 531.6 eV) peaks, which were both the main constituents of carboxylic groups. In addition, the presence of both $–NO_2$ (0.77 at%; 405.6 eV) and C–N (1.06 at%; 399.3 eV) peaks in the high-resolution N 1s spectrum of NCP–GC–COOH (Fig. 4(g)) reconfirms the nitrification of the carbon structure during surface oxidation by HNO_3 [39]. Similarly, the high-resolution O 1s (Fig. 4(f)) spectrum of NCP–GC–EDA shows that the C–O–H content dropped to 4.97 at% (from 8.22 at% in NCP–GC–COOH) and, contrarily, the C=O content increased to 7.09 at% (from 5.88 at% in NCP–GC–COOH). Moreover, two new amide/$–NH_2$ (5.28 at%, 399.8 eV) and $–NH_2$ (0.8 at%, 402.2 eV) peaks appeared in the high-resolution N 1s spectra of NCP–GC–EDA (Fig. 4(h)). These changes signal the formation of amide groups on the surface of NCP–GC–EDA after the cross-linking of polyamines on the carboxylic groups.

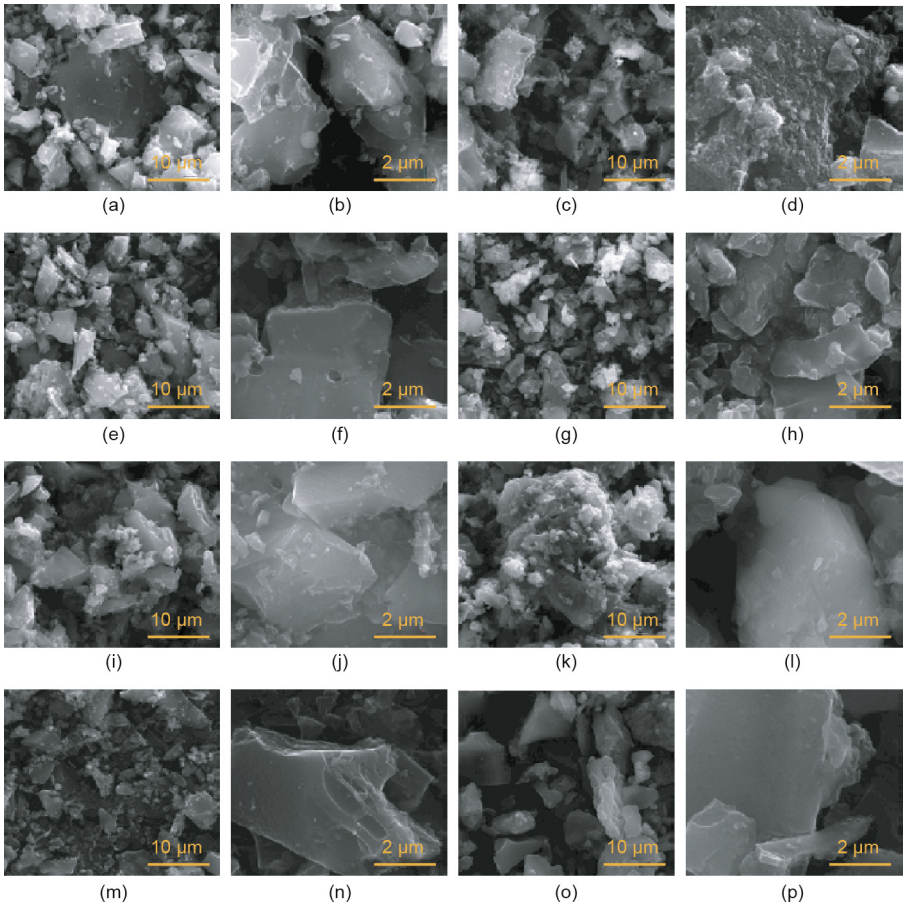

Fig. 5. SEM images of (a, b) microporous AC–GC and (c, d) mesoporous AC–GS carbon, (e, f) NCP–GC–COOH, (g, h) NCP–GS–COOH, (i, j) NCP–GC–EDA, (k, l) NCP–GS–EDA, (m, n) NCP–GC–PEI, and (o, p) NCP–GS–PEI promoters.

SEM images of the commercial activated carbons, oxidized carbon structures, and amine-functionalized NCPs are shown in Figs. 5 (a)–(p). The images show that the particle size of the carbon slightly decreased after HNO_3/H_2SO_4 treatment, which confirms that the carbon structure was broken down into smaller units after the harsh oxidation. However, the morphology remains nearly the same for all samples (either GC or GS structure) before and after the conjunction of different functional groups. Therefore, nitric acid oxidation does not affect the structural morphology of the NCP and no aggregation was observed after amine conjunction.

Fig. S4 in Appendix A shows the average particle size distribution of different NCPs obtained by DLS measurement. The results clearly confirm that all prepared NCP samples possessed an average diameter of less than 400 nm, which is much smaller than those displayed by SEM micrographs (1–2 μm). This discrepancy can be generally attributed to the differences in the operating mechanism of DLS and SEM characterizations. In SEM microscopy, characterization is performed in the solid state, which can strikingly accelerate the agglomeration of particles and increase the size of clusters. On the other hand, in the DLS technique, the particles are fully dispersed in solution using ultrasonication before starting the measurement, making DLS a better characterization method for determining the average particle size of similar systems.

3.2. Stability of NCP samples

To assess the stability of the synthesized NCPs, one of the most crucial characteristic factors of nanofluids, a zeta potential investigation was carried out. Figs. 6(a)–(h) shows the zeta potential values of all prepared DEEA–NCP nanofluids with different functionalities on the surface of the nanoporous promoters, along with photographs of their stability at different time intervals. In general, the zeta potential indicates the electrostatic charge (either attractive or repulsive) of solid particles/clusters suspended in a liquid phase. Therefore, the zeta potential value can indirectly represent the stability of suspended nanomaterials in nanofluids. Specifically, both very high (greater than 10 mV) and very low (less than −10 mV) zeta potential values can show that the suspended nanomaterials are thoroughly stable in solution. In contrast, values that fall between these extremes typically display nanomaterial instability and a tendency to agglomerate/precipitate. According to Figs. 6(a) and (b), as-prepared microporous NCP–GC–COOH (−33.42 mV) and mesoporous NCP–GS–COOH (−11.98 mV) exhibited high negative zeta potential values, which were attributed to the acidic functional groups (–COOH and –OH). Moreover, the zeta potential value of NCP-GC–COOH was about two times higher than that of the NCP–GS–COOH sample, which clearly shows that coconut-derived carbon is a better candidate for surface functionalization and NCP preparation than coal-derived carbon. As anticipated, the NCP–GC–COOH and NCP–GS–COOH promoters remained stable in suspension over a five-day period. After the conjunction of polyamines on the carboxylic groups through amide formation reaction, the zeta potential values increased due to the positive charges of the deprotonated amine groups. The strong positive charge of the polyamine groups on the surface of NCP–GC–PEI (−8.26 mV) and NCP–GS–EDA (−5.62 mV) elevated the particles' zeta potential to greater than −10 mV, resulting in

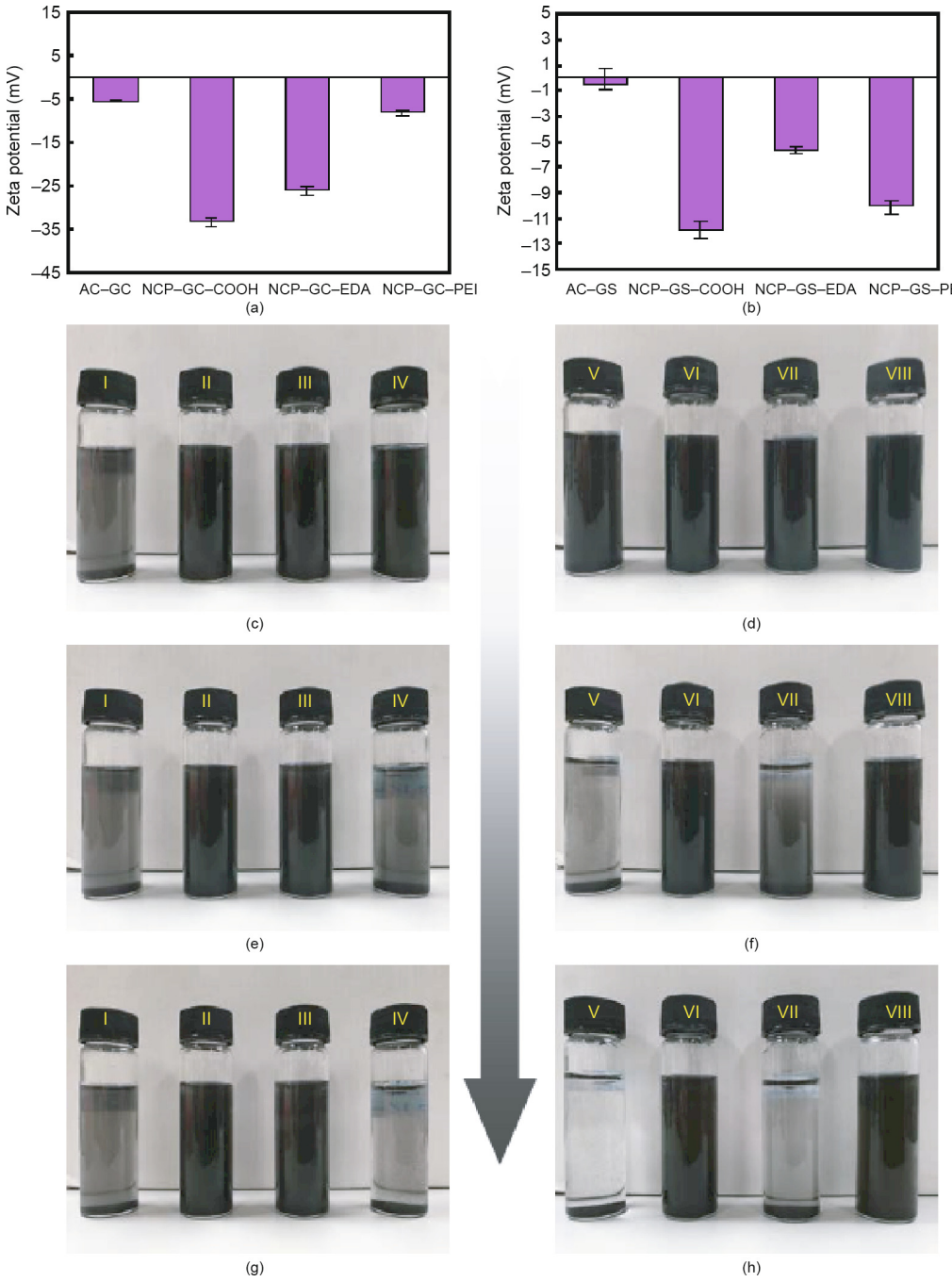

Fig. 6. Zeta potential analysis of prepared DEEA nanofluid containing different (a) GC and (b) GS carbon-based promoters; stability of (I) AC–GC, (II) NCP–GC–COOH, (III) NCP–GC–EDA, (IV) NCP–GC–PEI, (V) AC–GS, (VI) NCP–GS–COOH, (VII) NCP–GS–EDA, and (VIII) NCP–GS–PEI promoters at (c, d) 1 h, (e, f) 1 d, and (g, h) 5 d after sonication.

unstable suspensions (Figs. 6(g) and (h)). Conversely, the NCP–GC–EDA (−26.08 mV) and NCP–GS–PEI (−10.02 mV) promoters remained stable in the solution over a five-day period, due to optimum functional group distribution on the surface.

3.3. Kinetics of CO_2 absorption in DEEA–NCP nanofluids

As a tertiary amine, DEEA is unable to directly react with CO_2 molecules and generate carbamate. The reaction of tertiary amines with CO_2 is governed by an indirect hydrolysis reaction producing bicarbonate and protonated amine. As a result, most tertiary amines have a low rate of CO_2 absorption, which has hindered their prevalent utilization despite their considerable advantages (e.g., high absorption capacity and low heat of desorption). In this study, in order to quantify the role of different NCPs in the rate of CO_2 absorption in aqueous DEEA solutions, the pressure drop of CO_2 versus time for different DEEA–NCP nanofluids is provided in Figs. 7(a) and (b) Table S2 in Appendix A. Since PEI molecules contain many primary and secondary amine groups, it was expected that PEI-grafted NCP–GC–PEI and NCP–GS–PEI nanoporous promoters would exhibit a higher rate of CO_2 absorption compared with those containing EDA-grafted promoters with only one primary and one secondary amine site. Despite these expectations, DEEA–NCP nanofluids containing PEI-grafted NCPs exhibited a poorer CO_2 rate enhancement than those with EDA-grafted NCPs under similar conditions. According to Fig. 7(b), the CO_2 absorption curve of

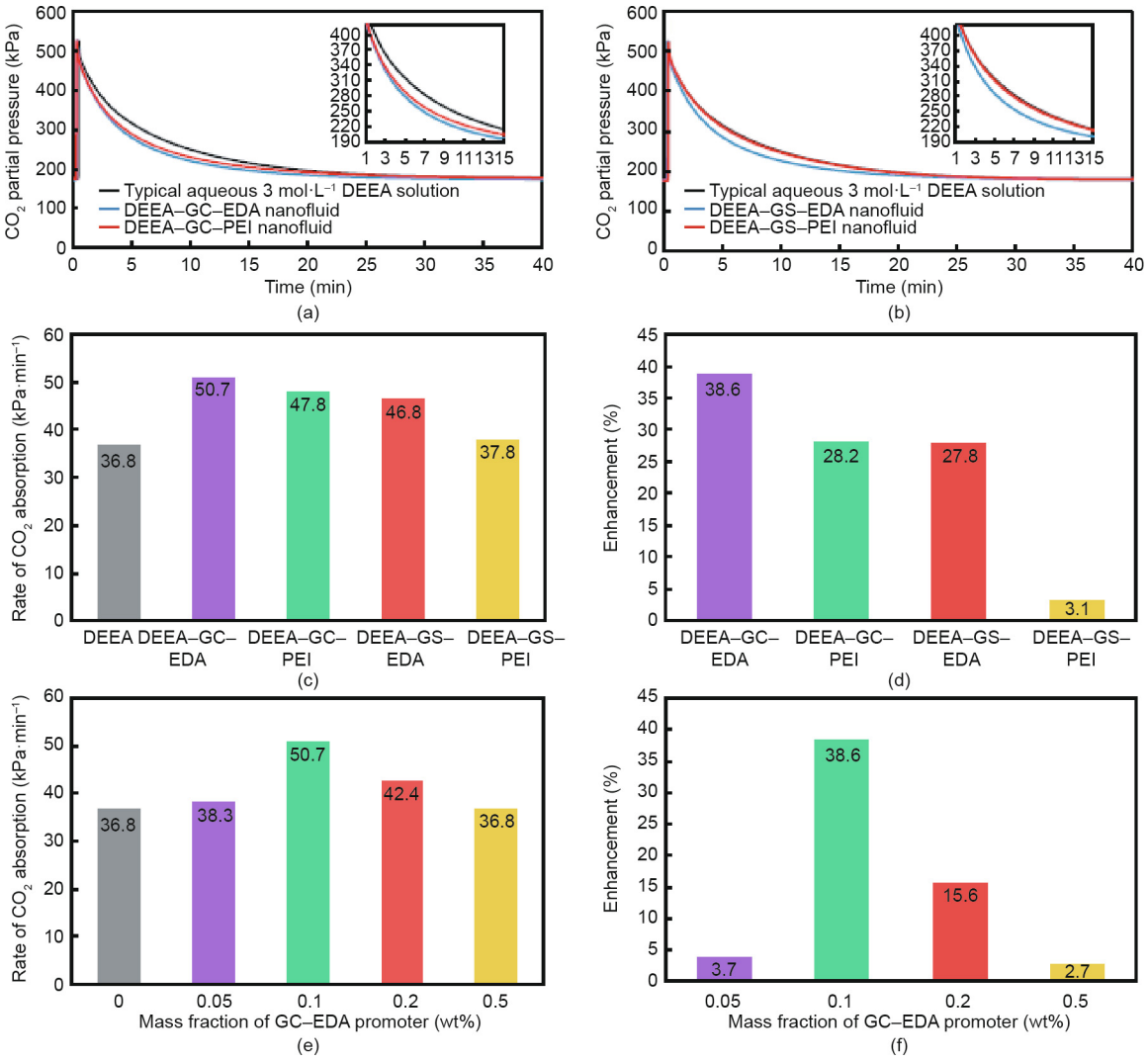

Fig. 7. (a, b) VLE experimental data of typical aqueous 3 mol·L^{-1} DEEA solution with (a) DEEA–GC–EDA and DEEA–GC–PEI and (b) DEEA–GS–EDA and DEEA–GS–PEI nanofluid at 40 °C and 0.1 wt% concentration of nano-promoter; (c) the rate of CO_2 absorption and (d) enhancement ratio for aqueous DEEA solution and DEEA–NCP nanofluids; the effect of GC–EDA promoter content on (e) the rate of CO_2 absorption and (f) enhancement ratio of DEEA–GC–EDA nanofluid at 40 °C.

DEEA–GS–PEI nanofluid had a considerable overlap with the typical DEEA solution across the whole absorption time period, confirming the poor performance of NCP–GS–PEI as a promoter. The low efficiency of PEI-grafted mesoporous DEEA–GS–PEI nanofluid demonstrated that the PEI molecules blocked the porous structure; as a result, most of the primary and secondary amine sites of the polyamine were nearly inaccessible in the DEEA–GS–PEI nanofluid, leading to insignificant reaction enhancement.

In contrast, nanofluids containing microporous promoters displayed superior performance compared with those containing mesoporous promoters, as demonstrated in Figs. 7(c) and (d) (also see Figs. S5 and S6 in Appendix A). Among all the prepared DEEA–NCP nanofluids, DEEA–GC–EDA nanofluid showed the best performance and succeeded in increasing the rate of CO_2 absorption to 50.7 kPa·min^{-1}, which is 38.6% greater than that of commercial DEEA solution (36.8 kPa·min^{-1}). Following this, in decreasing order were DEEA–GC–PEI (47.8 kPa·min^{-1}), DEEA–GS–EDA (46.6 kPa·min^{-1}), and DEEA–GS–PEI (37.8 kPa·min^{-1}), all of which improved the CO_2 absorption rate (by 28.2%, 27.8%, and 3.1%, respectively), in comparison with aqueous DEEA. Hence, the NCP–GC–EDA promoter with an EDA-grafted microporous structure was chosen as the best candidate among all synthesized NCPs with different properties. Therefore, it can be anticipated that using NCP–GC–EDA as a promotor for tertiary amine solutions can not only reduce the required residence time in the absorption column in order to reach a constant absorption capacity, but also decrease the solvent circulation rate and subsequently the amount of required energy for thermal regeneration.

3.4. Effect of NCP–GC–EDA concentration

As NCP–GC–EDA presented the best performance in CO_2 absorption rate enhancement among all screened microporous and mesoporous NCPs with different polyamine functionalities, the nanoporous NCP–GC–EDA promoter was selected to assess the role of carbonaceous promoter concentration on the rate of CO_2 absorption. To achieve this objective, DEEA–GC–EDA nanofluid with four different mass fractions of NCP–GC–EDA promoter (0.05 wt%, 0.1 wt%, 0.2 wt%, and 0.5 wt%) was analyzed for the concentration-dependent promotion of CO_2 absorption. Both the CO_2 absorption rate and the rate enhancement are presented in Figs. 7(e) and (f) (see also Fig. S7(a) in Appendix A). As shown in the figures, the presence of 0.05 wt% promoter in DEEA–GC–EDA nanofluid 3.7% increased (36.8 to 38.3 kPa·min^{-1}) the rate of CO_2

absorption. However, increasing the concentration of NCP–GC–EDA promoter to 0.1 wt% markedly increased the rate of CO_2 absorption in the nanofluid up to 50.7 kPa·min^{-1}, which was 38.6% more than that of aqueous DEEA solution without any promoter. Interestingly, the CO_2 absorption rate of both DEEA–GC–EDA nanofluids with 0.2 wt% (42.4 kPa·min^{-1}) and 0.5 wt% (36.8 kPa·min^{-1}) promoter was much less than that of DEEA–GC–EDA nanofluids with 0.1 wt% (50.7 kPa·min^{-1}). This adverse effect of NCP–GC–EDA promoter on the kinetics of CO_2 absorption can be related to the high viscosity of nanofluids at a high concentration of nanomaterials (see also Fig. S8 in Appendix A). This interpretation is consistent with the findings of Dharmalingam et al. [40], who reported the great influence of nanoparticles on the viscosity of nanofluids and their corresponding CO_2 absorption performance. According to Dharmalingam et al., the high concentration of nanomaterials in the aqueous solution can greatly increase the viscosity of the nanofluids, diminish the mass transfer coefficients at the gas–liquid interface, and suppress the positive effect of the promoter on the CO_2 absorption rate. Overall, this part of the study clearly suggested that adding nanoporous NCP–GC–EDA promoter with 0.1 wt% concentration as the optimum amount of promoter can substantially enhance the CO_2 absorption rate of aqueous DEEA solution, and indicated that using greater concentrations of GC–EDA should be avoided.

3.5. Absorption isotherms of CO_2 in DEEA–GC–EDA nanofluid

The CO_2 absorption capacity of both conventional aqueous 3 mol·L^{-1} DEEA solution and DEEA–GC–EDA nanofluid (3 mol·L^{-1}, 0.1 wt%) at different CO_2 partial pressures and 40 °C is provided in Fig. 8(a) (see also Table S3 and Table S4 in Appendix A). It can be seen that the trend of CO_2 absorption in both liquid absorbers was essentially identical and the solubility of CO_2 was raised by increasing the CO_2 partial pressure. Compared with conventional aqueous 3 mol·L^{-1} DEEA solution, the DEEA–GC–EDA nanofluid showed noticeably higher CO_2 absorption capacity over the range of CO_2 partial pressures (0.1–90 kPa), particularly at low CO_2 partial pressures. A simple comparison at a CO_2 partial pressure of 15 kPa (Fig. 8(b)) revealed that only the presence of 0.1 wt% NCP–GC–EDA promoter increased the CO_2 absorption capacity by 13.1% from 0.69 mol in aqueous DEEA solution to 0.78 mol CO_2 per mole DEEA in DEEA–GC–EDA nanofluid. In other words, DEEA–GC–EDA nanofluid has a CO_2 absorption capacity that is 13.1% higher than that of commercial aqueous DEEA solution for CO_2 from flue gas streams (at 15 kPa and 40 °C). With respect to the outcomes, the positive effect of NCP–GC–EDA promoter on the CO_2 absorption capacity is based on two factors. First, the porous structure of NCP–GC–EDA, which has a high surface area and pore volume, can physically adsorb a considerable amount of dissolved CO_2 molecules, CO_2-containing species, and protonated amines in the solvent, shift the bicarbonate formation reaction to the right side, and increase the equilibrium CO_2 absorption capacity in the whole system. Second, through the porous structure of NCP–GC–EDA, primary/secondary amine groups can effectively react with CO_2 molecules through carbamate formation reactions, facilitate the diffusion of CO_2 molecules into the nanoporous structure, and improve the final CO_2 absorption capacity of the solution. Although the DEEA–GC–EDA nanofluid maintained its CO_2 loading superiority over commercial aqueous DEEA solution, the CO_2 loading enhancement ratio gradually dropped from 13.1% at 15 kPa to 9.1% and 4.8% at 30 and 60 kPa, respectively. The better performance of NCP–GC–EDA promoter at low CO_2 partial pressures may be related to the fact that the effect of physical adsorption by the GC structure and the chemical promotion reaction by pri-

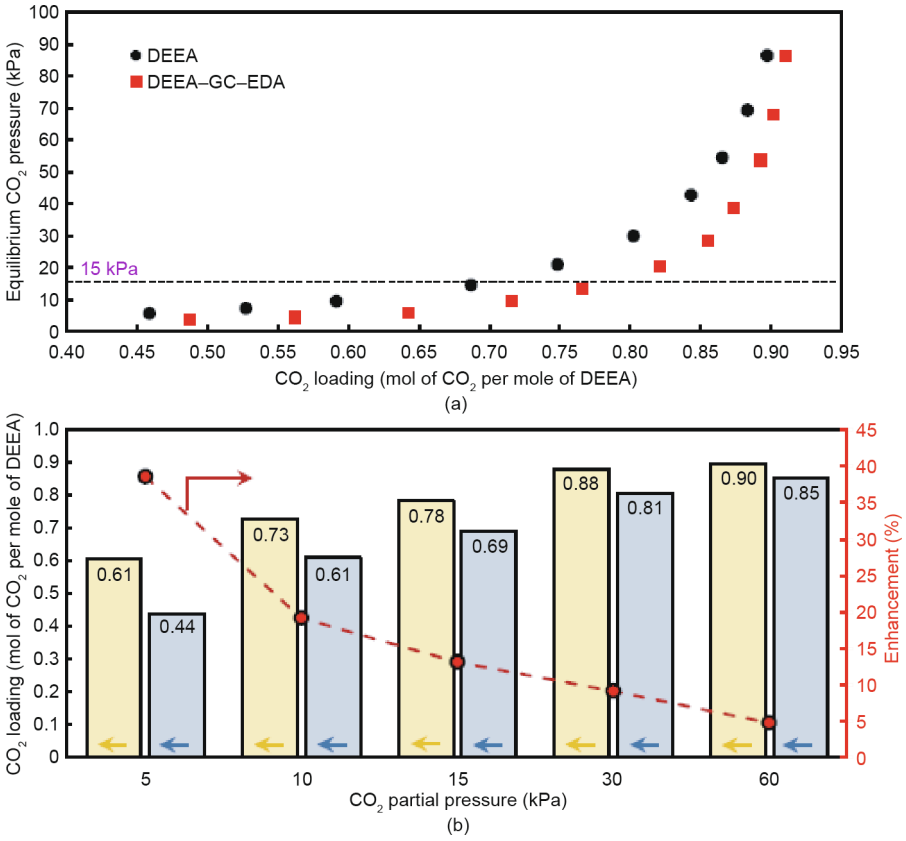

Fig. 8. Comparing (a) the CO_2 absorption isotherm, (b) equilibrium CO_2 loading and enhancement ratio of typical aqueous DEEA solution (grey) and DEEA–GC–EDA nanofluid (yellow).

mary/secondary amine sites inside the micropores is more significant at low CO_2 partial pressures.

To evaluate the stability of nanoporous NCP–GC–EDA as a newly introduced CO_2 promoter, the CO_2 absorption rate, CO_2 rate enhancement compared with aqueous DEEA solution, and regeneration efficiency of DEEA–GC–EDA nanofluid during three consecutive absorption–desorption cycles were measured (Fig. 9(a)). As shown in Fig. 9(a), the regeneration efficiency dropped to 96.19% during the first cycle, resulting in a CO_2 absorption rate reduction from 50.70 kPa·min^{-1} (38.6% enhancement) to 48.77 kPa·min^{-1} (32.88% enhancement). This reduction can be attributed to the partial distortion (or saturation) of amine sites and blockage of the GC structure due to the irreversible physical absorption and chemical reaction between CO_2 and primary amine groups on the surface. In a similar trend, the rate of CO_2 absorption and regeneration efficiency gradually declined to 47.89 kPa·min^{-1} and 94.46% during the second cycle, and reached 48.06 kPa·min^{-1} and 94.79% in the third cycle. Due to the similar regeneration efficiency values in the second and third cycles, it was assumed that the cyclic CO_2 absorption rate of DEEA–GC–EDA nanofluid stabilized after three successive cycles. Analyzing the data revealed that the cyclic CO_2 absorption rate of DEEA–GC–EDA nanofluid was only 5.2% (50.7 to 48.06 kPa·min^{-1}) less than its initial CO_2 absorption rate, which shows the high performance of nanoporous NCP–GC–EDA during cyclic CO_2 absorption–desorption operation. Thus, NCP–GC–EDA promoter can be easily used for large-scale CO_2 absorption from flue gas using aqueous tertiary amine solutions.

To investigate the promotion mechanism of microporous NCP–GC–EDA in aqueous DEEA solution during CO_2 absorption, CO_2-saturated DEEA–GC–EDA nanofluid was centrifuged (10 000, 15 min) and the remaining brownish supernatant was characterized by FT-IR and NMR spectroscopy. FT-IR, ^{13}C NMR, and ^{1}H NMR spectra of CO_2-saturated DEEA–GC–EDA nanofluid, CO_2-saturated DEEA solution without using any promoter, and fresh aqueous DEEA solution (before CO_2 absorption) are depicted in Figs. 9(b) and (c) and Fig. S7(b) in Appendix A. A comparison between the FT-IR spectra of different samples disclosed that both the aqueous DEEA solution and the DEEA–GC–EDA nanofluid contained similar species. The increase in the intensity of the absorption bands in the 1350–1360 and 1560–1625 cm^{-1} regions is related to the formation of bicarbonate and protonated amine during CO_2 absorption [41]. Also, the ^{1}H NMR and ^{13}C NMR spectra of different samples displayed similar results to those of FT-IR and confirmed the presence of bicarbonate as the only CO_2-containing species in the solution. It is worth noting that both characterization methods emphasized that no carbamate formed in the solution during CO_2 absorption. This finding implies that using carbonaceous NCP–GC–EDA promoter does not influence the CO_2 absorption mechanism in tertiary amine solutions, and that the reaction is governed by direct bicarbonate formation reaction. Hereupon, it can be deduced that nanoporous NCP–GC–EDA can promote the rate of CO_2 absorption and equilibrium CO_2 absorption capacity of tertiary amines through a direct carbamate formation reaction between physically absorbed CO_2 molecules and the primary/secondary amine groups of grafted polyamines in the nanoporous structure of NCPs.

4. Conclusions

In summary, a novel nanoporous rate promoter with polyamine functional groups was introduced to enhance the rate of CO_2 absorption in aqueous tertiary amines. To assess the roles of textural porosity and amine functional groups, both GC and GS carbon structures were employed and post-functionalized by EDA and PEI molecules as typical polyamines with low and high molecular weight, respectively. All synthesized NCPs were fully characterized by FT-IR, XPS, TGA, Raman, SEM, and elemental analysis to evaluate

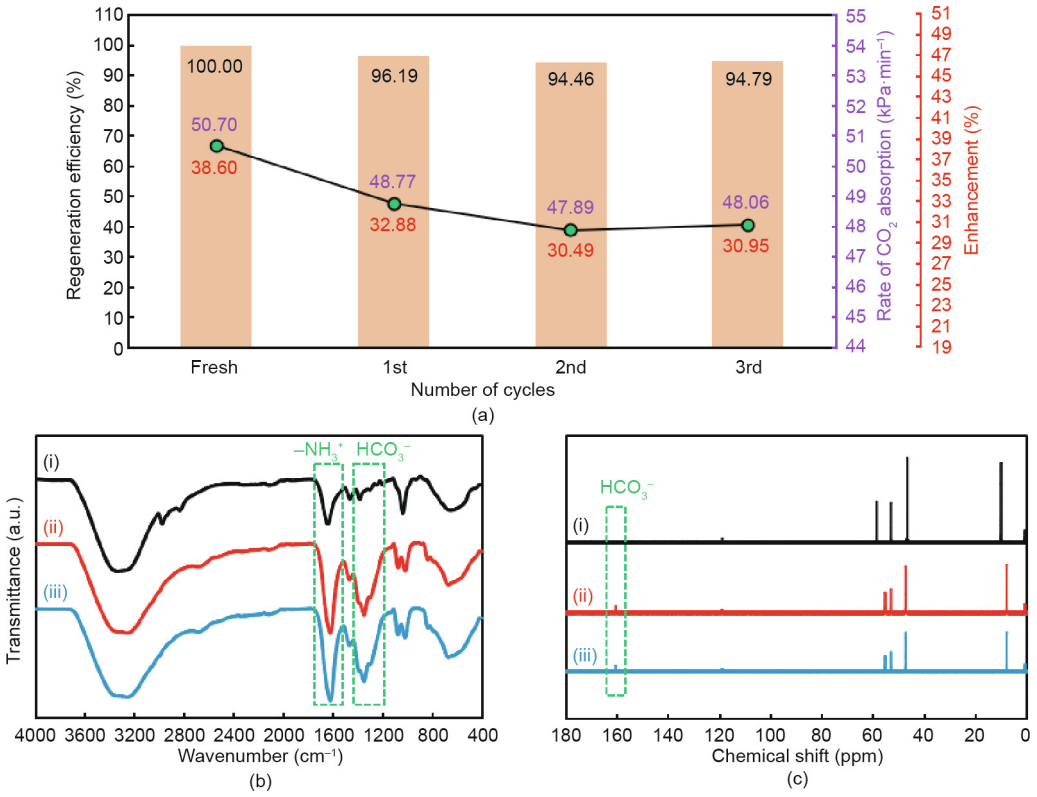

Fig. 9. (a) Rate of CO_2 absorption, regeneration efficiency and enhancement ratio of DEEA–GC–EDA nanofluid over three consecutive cycles; (b) FT-IR and (c) ^{13}C NMR of fresh aqueous DEEA solution (i) before and (ii) after CO_2 absorption, and (iii) DEEA–GC–EDA nanofluid after CO_2 absorption.

the structure of the promoters. The results of CO_2 absorption in aqueous DEEA–NCP nanofluids confirmed that DEEA–GC–EDA nanofluid containing EDA-grafted GC structures displayed the most promising performance among all prepared nanofluids. To be specific, the use of only 0.1 wt% of NCP–GC–EDA promoter in a typical aqueous DEEA solution succeeded in improving the rate of CO_2 absorption from 36.8 to 50.7 kPa·min^{-1} (38.6%) and the equilibrium CO_2 absorption capacity from 0.69 to 0.78 mol CO_2 per mole DEEA (13.2%). Moreover, the effect of NCP–GC–EDA concentration on the kinetics of CO_2 absorption was studied, and it was demonstrated that 0.1 wt% is the optimum amount of NCP in the aqueous DEEA solution. To assess the recyclability of NCP–GC–EDA, the cyclic CO_2 absorption rate of DEEA–GC–EDA nanofluid was measured, which only displayed 5.2% (50.7–48.06 kPa·min^{-1}) reduction over three successive CO_2 absorption–desorption cycles. In addition, an enhancement mechanism was suggested for the NCP–GC–EDA rate promoter based on the FT-IR and NMR spectroscopy before and after CO_2 absorption in DEEA–GC–EDA nanofluid. Overall, the microporous NCP–GC–EDA structure can be proposed as a viable promoter to effectively overcome the drawbacks of tertiary amine solutions, in order to enhance the rate of CO_2 absorption and facilitate their large-scale utilization.

Acknowledgements

The authors would like to acknowledge the University of Melbourne for the Melbourne Research Scholarship, infrastructural support, and financial resources provided for this project. The authors also acknowledge the support of the Bio21 Advanced Microscopy Facility (the University of Melbourne) and Melbourne TrACEES Platform (Trace Analysis for Chemical, Earth and Environmental Sciences) for the technical support, data analysis, and expert advice.

Compliance with ethics guidelines

Masood S. Alivand, Omid Mazaheri, Yue Wu, Geoffrey W. Stevens, Colin A. Scholes, and Kathryn A. Mumford declare that they have no conflict of interest or financial conflicts to disclose.

Appendix A. Supplementary data

Supplementary data to this article can be found online at https://doi.org/10.1016/j.eng.2020.05.004.

References

[1] Alivand MS, Shafiei-Alavijeh M, Tehrani NHMH, Ghasemy E, Rashidi A, Fakhraie S. Facile and high-yield synthesis of improved MIL-101(Cr) metal–organic framework with exceptional CO_2 and H_2S uptake; the impact of excess ligand-cluster. Microporous Mesoporous Mater 2019;279:153–64.
[2] Zhang X, Zhu Z, Sun X, Yang J, Gao H, Huang Y, et al. Reducing energy penalty of CO_2 capture using Fe promoted SO_4^{2-}/ZrO_2/MCM-41 catalyst. Environ Sci Technol 2019;53(10):6094–102.
[3] Lai Q, Toan S, Assiri MA, Cheng H, Russell AG, Adidharma H, et al. Catalyst-$TiO(OH)_2$ could drastically reduce the energy consumption of CO_2 capture. Nat Commun 2018;9(1):1–7.
[4] Wang L, Liu S, Wang R, Li Q, Zhang S. Regulating phase separation behavior of a DEEA−TETA biphasic solvent using sulfolane for energy-saving CO_2 capture. Environ Sci Technol 2019;53(21):12873–81.
[5] Alivand MS, Mazaheri O, Wu Y, Stevens GW, Scholes CA, Mumford KA. Development of aqueous-based phase change amino acid solvents for energy-efficient CO_2 capture: the role of antisolvent. Appl Energy 2019;256:113911.
[6] Gao H, Xu B, Liu H, Liang Z. Effect of amine activators on aqueous *N,N*-diethylethanolamine solution for postcombustion CO_2 capture. Energy Fuels 2016;30(9):7481–8.
[7] Wu Y, Alivand MS, Hu G, Stevens GW, Mumford KA. Nucleation kinetics of glycine promoted concentrated potassium carbonate solvents for carbon dioxide absorption. Chem Eng J 2020;381:122712.
[8] Tehrani NHMH, Alivand MS, Maklavany DM, Rashidi A, Samipoorgiri M, Seif A, et al. Novel asphaltene-derived nanoporous carbon with N-S-rich micro-mesoporous structure for superior gas adsorption: experimental and DFT study. Chem Eng J 2019;358:1126–38.
[9] Alivand MS, Farhadi F. Multi-objective optimization of a multi-layer PTSA for LNG production. J Nat Gas Sci Eng 2018;49:435–46.
[10] Alivand MS, Tehrani NHMH, Shafiei-Alavijeh M, Rashidi A, Kooti M, Pourreza A, et al. Synthesis of a modified HF-free MIL-101(Cr) nanoadsorbent with enhanced H_2S/CH_4, CO_2/CH_4, and CO_2/N_2 selectivity. J Environ Chem Eng 2019;7(2):102946.
[11] Miandoab ES, Kentish SE, Scholes CA. Non-ideal modelling of polymeric hollow-fibre membrane systems: pre-combustion CO_2 capture case study. J Membrane Sci 2020;595:117470.
[12] Hosseini E, Stevens GW, Scholes CA. Membrane gas-solvent contactors undergoing oscillating solvent flow for enhanced carbon dioxide capture. Sep Purif Technol 2019;227:115653.
[13] Fronk BM, Garimella S. Condensation of carbon dioxide in microchannels. Int J Heat Mass Transfer 2016;100:150–64.
[14] Sun W, Cao X, Yang W, Jin X. Numerical simulation of CO_2 condensation process from CH_4–CO_2 binary gas mixture in supersonic nozzles. Sep Purif Technol 2017;188:238–49.
[15] Bhatti UH, Nam S, Park S, Baek IH. Performance and mechanism of metal oxide catalyst-aided amine solvent regeneration. ACS Sustainable Chem Eng 2018;6(9):12079–87.
[16] Zhang Z, Cai J, Chen F, Li H, Zhang W, Qi W. Progress in enhancement of CO_2 absorption by nanofluids: a mini review of mechanisms and current status. Renewable Energy 2018;118:527–35.
[17] Cui M, Chen S, Qi T, Zhang Y. Investigation of CO_2 capture in nonaqueous ethylethanolamine solution mixed with porous solids. J Chem Eng Data 2018;63(5):1198–205.
[18] Song Y, Cao L, Yu J, Zhang S, Chen S, Jiang Y. Amino-functionalized graphene oxide blend with monoethanolamine for efficient carbon dioxide capture. J Alloy Compd 2017;704:245–53.
[19] Hafizi A, Mokari MH, Khalifeh R, Farsi M, Rahimpour MR. Improving the CO_2 solubility in aqueous mixture of MDEA and different polyamine promoters: the effects of primary and secondary functional groups. J Mol Liq 2020;297:111803.
[20] Irani V, Tavasoli A, Vahidi M. Preparation of amine functionalized reduced graphene oxide/methyl diethanolamine nanofluid and its application for improving the CO_2 and H_2S absorption. J Colloid Interf Sci 2018;527:57–67.
[21] Vaidya PD, Kenig EY. Absorption of CO_2 into aqueous blends of alkanolamines prepared from renewable resources. Chem Eng Sci 2007;62(24):7344–50.
[22] Chowdhury FA, Yamada H, Higashii T, Goto K, Onoda M. CO_2 capture by tertiary amine absorbents: a performance comparison study. Ind Eng Chem Res 2013;52(24):8323–31.
[23] Chowdhury FA, Okabe H, Shimizu S, Onoda M, Fujioka Y. Development of novel tertiary amine absorbents for CO_2 capture. Energy Procedia 2009;1(1):1241–8.
[24] Rahmatmand B, Keshavarz P, Ayatollahi S. Study of absorption enhancement of CO_2 by SiO_2, Al_2O_3, CNT, and Fe_3O_4 nanoparticles in water and amine solutions. J Chem Eng Data 2016;61(4):1378–87.
[25] Komati S, Suresh AK. CO_2 absorption into amine solutions: a novel strategy for intensification based on the addition of ferrofluids. J Chem Technol Biotechnol 2008;83(8):1094–100.
[26] Maleki A, Irani V, Tavasoli A, Vahidi M. Enhancement of CO_2 solubility in a mixture of 40 wt% aqueous *n*-methyldiethanolamine solution and diethylenetriamine functionalized graphene oxide. J Nat Gas Sci Eng 2018;55:219–34.
[27] Alivand MS, Mazaheri O, Wu Y, Stevens GW, Scholes CA, Mumford KA. Data in brief on CO_2 absorption–desorption of aqueous-based amino acid solvents with phase change behaviour. Data Brief 2019;27:104741.
[28] Tehrani NHMH, Alivand MS, Rashidi A, Shamskar KR, Samipoorgiri M, Esrafili MD, et al. Preparation and characterization of a new waste-derived mesoporous carbon structure for ultrahigh adsorption of benzene and toluene at ambient conditions. J Hazard Mater 2020;384:121317.
[29] Alivand MS, Najmi M, Tehrani NHMH, Kamali A, Tavakoli O, Rashidi A, et al. Tuning the surface chemistry and porosity of waste-derived nanoporous materials toward exceptional performance in antibiotic adsorption: experimental and DFT studies. Chem Eng J 2019;374:274–91.
[30] Babu CM, Binnemans K, Roosen J. Ethylenediaminetriacetic acid-functionalized activated carbon for the adsorption of rare earths from aqueous solutions. Ind Eng Chem Res 2018;57(5):1487–97.
[31] Shin YR, Jeon IY, Baek JB. Stability of multi-walled carbon nanotubes in commonly used acidic media. Carbon 2012;50(4):1465–76.
[32] Li S, Amat D, Peng Z, Vanni S, Raskin S, De Angulo G, et al. Transferrin conjugated nontoxic carbon dots for doxorubicin delivery to target pediatric brain tumor cells. Nanoscale 2016;8(37):16662–9.
[33] Thiruselvi T, Thirupathi KRS, Aravindhan R, Shanuja SK, Gnanamani A. Handling and managing bleeding wounds using tissue adhesive hydrogel: a comparative assessment on two different hydrogels. RSC Adv 2016;6(24):19973–81.
[34] De Sousa M, Martins CHZ, Franqui LS, Fonseca LC, Delite FS, Lanzoni EM, et al. Covalent functionalization of graphene oxide with *D*-mannose: evaluating the hemolytic effect and protein corona formation. J Mater Chem B 2018;6(18):2803–12.
[35] You YZ, Yan JJ, Yu ZQ, Cui MM, Hong CY, Qu BJ. Multi-responsive carbon nanotube gel prepared via ultrasound-induced assembly. J Mater Chem 2009;19(41):7656–60.

[36] Yue YN, Meng WJ, Liu L, Hu QL, Wang H, Lu JX. Amino acid-functionalized multi-walled carbon nanotubes: a metal-free chiral catalyst for the asymmetric electroreduction of aromatic ketones. Electrochim Acta 2018;260:606–13.
[37] Rosca ID, Watari F, Uo M, Akasaka T. Oxidation of multiwalled carbon nanotubes by nitric acid. Carbon 2005;43(15):3124–31.
[38] Arshadi M, Taghvaei H, Abdolmaleki MK, Lee M, Eskandarloo H, Abbaspourrad A. Carbon dioxide absorption in water/nanofluid by a symmetric amine-based nanodendritic adsorbent. Appl Energy 2019;242:1562–72.
[39] Tchoul MN, Ford WT, Lolli G, Resasco DE, Arepalli S. Effect of mild nitric acid oxidation on dispersability, size, and structure of single-walled carbon nanotubes. Chem Mater 2007;19(23):5765–72.
[40] Dharmalingam S, Park KT, Lee JY, Park IG, Jeong SK. Catalytic effect of metal oxides on CO_2 absorption in an aqueous potassium salt of lysine. J Ind Eng Chem 2018;68:335–41.
[41] Mohsin HM, Johari K, Shariff AM. Virgin coconut oil (VCO) and potassium glycinate (PG) mixture as absorbent for carbon dioxide capture. Fuel 2018;232:454–62.